



AFRL-RX-WP-JA-2017-0199

CNT-BASED ARTIFICIAL HAIR SENSORS FOR PREDICTABLE BOUNDARY LAYER AIR FLOW SENSING (POSTPRINT)

**Jeffery W. Baur
AFRL/RX**

**Keith A. Slinker and Corey Kondash
Universal Technologies Corporation**

**Benjamin T. Dickinson
AFRL/RW**

**22 July 2016
Interim Report**

**Distribution Statement A.
Approved for public release: distribution unlimited.**

© 2016 WILEY-VCH

(STINFO COPY)

**AIR FORCE RESEARCH LABORATORY
MATERIALS AND MANUFACTURING DIRECTORATE
WRIGHT-PATTERSON AIR FORCE BASE, OH 45433-7750
AIR FORCE MATERIEL COMMAND
UNITED STATES AIR FORCE**

REPORT DOCUMENTATION PAGE				Form Approved OMB No. 0704-0188
<p>The public reporting burden for this collection of information is estimated to average 1 hour per response, including the time for reviewing instructions, searching existing data sources, gathering and maintaining the data needed, and completing and reviewing the collection of information. Send comments regarding this burden estimate or any other aspect of this collection of information, including suggestions for reducing this burden, to Department of Defense, Washington Headquarters Services, Directorate for Information Operations and Reports (0704-0188), 1215 Jefferson Davis Highway, Suite 1204, Arlington, VA 22202-4302. Respondents should be aware that notwithstanding any other provision of law, no person shall be subject to any penalty for failing to comply with a collection of information if it does not display a currently valid OMB control number. PLEASE DO NOT RETURN YOUR FORM TO THE ABOVE ADDRESS.</p>				
1. REPORT DATE (<i>DD-MM-YY</i>) 22 July 2016		2. REPORT TYPE Interim		3. DATES COVERED (<i>From - To</i>) 22 July 2013 – 22 June 2016
4. TITLE AND SUBTITLE CNT-BASED ARTIFICIAL HAIR SENSORS FOR PREDICTABLE BOUNDARY LAYER AIR FLOW SENSING (POSTPRINT)				5a. CONTRACT NUMBER IN-HOUSE
				5b. GRANT NUMBER
				5c. PROGRAM ELEMENT NUMBER
6. AUTHOR(S) 1) Jeffery W. Baur – AFRL/RX		2) Keith A. Slinker and Corey Kondash - Universal Technologies Corporation		5d. PROJECT NUMBER
				5e. TASK NUMBER
				5f. WORK UNIT NUMBER X0S7
7. PERFORMING ORGANIZATION NAME(S) AND ADDRESS(ES) 1) AFRL/RX Wright-Patterson AFB, OH 45433		2) Universal Technologies Corporation 1270 N. Fairfield Rd, Dayton OH 45432		8. PERFORMING ORGANIZATION REPORT NUMBER
				(Continued on page 2)
9. SPONSORING/MONITORING AGENCY NAME(S) AND ADDRESS(ES) Air Force Research Laboratory Materials and Manufacturing Directorate Wright-Patterson Air Force Base, OH 45433-7750 Air Force Materiel Command United States Air Force				10. SPONSORING/MONITORING AGENCY ACRONYM(S) AFRL/RXCC
				11. SPONSORING/MONITORING AGENCY REPORT NUMBER(S) AFRL-RX-WP-JA-2017-0199
12. DISTRIBUTION/AVAILABILITY STATEMENT Distribution Statement A. Approved for public release: distribution unlimited.				
13. SUPPLEMENTARY NOTES PA Case Number: 88ABW-2016-3588; Clearance Date: 22 July 2016. This document contains color. Journal article published in Advanced Materials Technologies, Vol. 1, 7 Nov 2016. © 2016 Wiley-VCH. The U.S. Government is joint author of the work and has the right to use, modify, reproduce, release, perform, display, or disclose the work. The final publication is available at wileyonlinelibrary.com DOI: 10.1002/admt.201600176				
14. ABSTRACT (<i>Maximum 200 words</i>) While numerous flow sensor architectures mimic the natural cilia of crickets, locusts, bats, and fish, the prediction of sensor output for given flow conditions based on the sensor properties has not been achieved. Challenges include difficulty in determining the electromechanical properties of the sensors, limited working knowledge of the boundary layer, low sensitivity to small hair deflections, and lack of models for large deflections. Within this work, hair sensors are fabricated using piezoresistive arrays of carbon nanotubes (CNTs) without traditional microelectromechanical processing. While correlating the CNT array electromechanical properties to synthesis conditions remains a challenge, a consistent, proportional, and predictable response to steady, boundary-determined air flow is obtained using theory and measurement for various lengths of hairs. The moment sensitivity is shown to scale inversely with the CNT length and stiffness to a typical maximum of $1.3 \pm 0.4\%$ resistance change $nN^{-1} m^{-1}$. The normalized CNT piezoresistivity is constant (1.1 ± 0.2) for a majority of the more than two dozen sensors examined despite the orders-of-magnitude variability in both sensitivity and CNT compressive modulus.				
15. SUBJECT TERMS flow sensor architectures ; hair sensor; piezoresistive array; carbon nanotubes (CNTs); hair deflection				
16. SECURITY CLASSIFICATION OF: a. REPORT Unclassified		17. LIMITATION OF ABSTRACT: b. ABSTRACT Unclassified c. THIS PAGE Unclassified	18. NUMBER OF PAGES 14	19a. NAME OF RESPONSIBLE PERSON (Monitor) William Kennedy 19b. TELEPHONE NUMBER (Include Area Code) (937) 255-9987

REPORT DOCUMENTATION PAGE Cont'd

6. AUTHOR(S)

3) Benjamin T. Dickinson - AFRL/RW

7. PERFORMING ORGANIZATION NAME(S) AND ADDRESS(ES)

3) AFRL/RW
Eglin AFB, FL 32542

CNT-Based Artificial Hair Sensors for Predictable Boundary Layer Air Flow Sensing

Keith A. Slinker,* Corey Kondash, Benjamin T. Dickinson, and Jeffery W. Baur

While numerous flow sensor architectures mimic the natural cilia of crickets, locusts, bats, and fish, the prediction of sensor output for given flow conditions based on the sensor properties has not been achieved. Challenges include difficulty in determining the electromechanical properties of the sensors, limited working knowledge of the boundary layer, low sensitivity to small hair deflections, and lack of models for large deflections. Within this work, hair sensors are fabricated using piezoresistive arrays of carbon nanotubes (CNTs) without traditional microelectromechanical processing. While correlating the CNT array electromechanical properties to synthesis conditions remains a challenge, a consistent, proportional, and predictable response to steady, boundary-determined air flow is obtained using theory and measurement for various lengths of hairs. The moment sensitivity is shown to scale inversely with the CNT length and stiffness to a typical maximum of $1.3 \pm 0.4\%$ resistance change $nN^{-1} m^{-1}$. The normalized CNT piezoresistivity is constant (1.1 ± 0.2) for a majority of the more than two dozen sensors examined despite the orders-of-magnitude variability in both sensitivity and CNT compressive modulus. The sensor sensitivity and noise both distinctly change as the flow transitions from steady and laminar to turbulent, suggesting the sensor may be capable of detecting flow transitions.

1. Introduction

Microscale sensors with a hair or cilium that extends out of plane into the oncoming flow have been shown to be effective for detecting fluid flow (i.e., air or water) over a surface. Quantifiably predicting their response requires knowledge and valid assumptions about the spatial variation of the flow across the surface of the cilium (e.g., a boundary layer profile), the expected

interaction of the air with the cilium (or drag force from the drag coefficient), how the forces on the cilium are translated into the transducing element, and the electrical response of the transducer to the translated strain (i.e., the gauge factor).^[1-4] One might be able to calibrate the response of a sensor to known flow conditions without the knowledge of their internal mechanics; however, this is laborious, capital intensive, and only provides information for limited conditions. The drift sometimes observed in micro-scale, strain-based sensors can present additional difficulty in interpreting their response over long timescales or under varying conditions. Schemes may be required for both normalizing and zeroing of data in order to correlate between measured and calibrated responses. With sufficient understanding of the air flow conditions and the inner electromechanics of a cilium sensor, it should be possible to directly predict the response of the sensor or extrapolate from simple, laboratory-scale calibration

measurements to a wide variety of flow conditions. Given such validated correlation between structure–property models and performance, ranges of reliable operation can be established and the sensors can be tuned for response in a desired flow regime.

Most of the artificial cilium sensors for which some sort of correlation has been attempted have been fabricated by microelectromechanical (MEMS) processes in three general types: silicon cantilevers that are curled out-of-plane,^[5,6] silicon platens attached or fabricated perpendicular to silicon cantilevers,^[1,2,7] and cylindrical polymer hairs attached perpendicular to silicon cantilevers, polymeric slabs, or tilting plates.^[8-13] While the remainder of these devices have piezoresistive or piezoelectric transducers at the base of the cantilever or across the slab, much work has been done on a hair-on-tilting-plate device with a capacitive transducer that seems to be well suited for detecting dynamic (“AC”) rather than steady airflows.^[9,10] The developers of these devices assume the same model put forward by Shimozawa et al. for cricket hairs. The “drag moment” which results from the external drag forces acting over the length of the exposed hair is balanced by the restoring momentum due to angular motion of the hair, a function of the torsional resistance and spring stiffness of the base.^[11] They developed a model for the gauge factor—relating the output capacitance to the rotational angle of the hair—and verified their correlation

Dr. K. A. Slinker, C. Kondash
Universal Technology Corporation
Materials and Manufacturing Directorate
Air Force Research Laboratory
2941 Hobson Way, Wright-Patterson Air Force Base
OH 45433, USA
E-mail: keith.slinker.ctr@us.af.mil

Dr. B. T. Dickinson
Munitions Directorate
Air Force Research Laboratory
101 W Eglin Blvd, Eglin Air Force Base, FL 32542, USA

Dr. J. W. Baur
Materials and Manufacturing Directorate Air
Force Research Laboratory
2941 Hobson Way, Wright-Patterson Air Force Base
OH 45433, USA

DOI: 10.1002/admt.201600176



of the expected AC boundary layer profile and AC drag forces to the motion of the hair through direct optical observation.^[9,12] Measuring the response in an air flow tube, they showed that their devices respond to both drag forces through the cilium as well as pressure presumably acting directly on the tilting plate which may make it difficult to discriminate between changes in surface pressure and changes in boundary layer velocity profile.^[14] More recently, Nima and Stephen used a similar approach to model the AC response of their glass fiber hairs with multi-droplet interface bi-layer transducers, differing by about a factor of 3 from their experimental measurements under specialized air flow conditions.^[15]

Regarding quasi-static flow sensing, early efforts by both Ozaki et al. and Fan et al. note that the strain on the transducing region of cantilever devices should be proportional to the drag moment on the device, but neither attempted to correlate their models to their device responses.^[1,2] Zhang et al. treated the drag coefficient as an unknown in modeling their uniform-width, curled cantilevers for water flow sensing.^[6] They calibrated the response of the sensors under controlled flow conditions to determine the drag coefficient. After normalizing for drift, the modeled response using their drag coefficient agreed to within 10% when comparing back to the calibration data or for a second sensor.

Air flow detection may prove more difficult than water flow detection as the typical boundary layer is five times thicker and the drag force is 40 times lower.^[16,17] Indeed, the flow sensing cilia on spiders are significantly longer than those found on fish. Wang et al. tested their curled cantilever devices under quasi-static air flow with good correlation between their predicted and measured sensor response, but the cantilevers did not extend significantly out of the surface and were sensitive to pressure rather than boundary layer flow.^[5] Du et al. fabricated in-plane cantilevers, then mounted the entire chip transverse to the air flow outside the boundary layer to achieve drag detection of the uniform, freestream air flow.^[7] They calculated the expected strain for a given drag moment and the gauge factor directly from literature material properties. Without indicating the drag coefficient they assumed, their model agreed with the measured response within about 30%. Kottapalli et al. demonstrated an increase in sensitivity by adding a cupula of specific geometry to their polycarbonate hairs fabricated on conformable liquid crystal polymer slabs capped with a thin gold strain gauge.^[13] Similar to Du et al., they tested their sensors in the freestream flow at the center of a wind tunnel, and their model approximating the differences predicted the enhancements in drag force to within a factor of 2. Chen et al. mounted their hair-on-cantilever device on a surface and assumed a flat-plate to approximate the boundary layer profile.^[8] They calibrated the piezoresistive gauge factor by deflecting the tip of the hair and treated the hair as an infinite cylinder for estimating the drag coefficient. They were able to reproduce the trend of the response to boundary-layer air flow but underestimated the magnitude by about a factor of 5. Overall, the moderate to low sensitivity of MEMS flow sensors and the lack of control over their air flow testing environments have limited the demonstration of quantifiable detection of quasi-static air flow. Additionally, the challenge of knowing or measuring the structural and transducing properties of the constituent elements of these

devices has prevented the direct prediction of response based on device design even for simple changes such as to the length of the hair.

Alternatively, artificial hair sensors (AHS) have also been fabricated by MEMS-free processes from high stiffness structural glass microfibers and carbon nanotubes (CNTs).^[18,19] The CNTs in these devices form self-aligned, radial arrays during synthesis that have been shown to exhibit elastic, foam-like behavior and large piezoresistance in response to compressive strain against a conductive surface.^[20–22] This native piezoresistance is thought to be a combination of increased connectivity of the CNTs with the contacting surface as well as increased tube-to-tube connectivity as the array is compressed, but its magnitude cannot yet be predicted *a priori*. In these sensors, the CNT array both mechanically supports the fiber and transduces the motion of the fiber into a change in resistance. The CNT-based AHS have been shown to have high sensitivity in comparison to other hair sensor devices and in their ability to detect the separation and stagnation points in air flow over a cylinder.^[18,19]

Here we discuss the fabrication, characterization, and modeling of these CNT-based artificial hair sensors in the context of predicting and measuring their response to quasi-static changes in air flow. Previously, these sensors have also been shown to have a large bandwidth and predictable response to dynamic perturbations, but modeling of those responses will not be discussed here.^[23,24] We show through both theory and measurement that the response for this sensor architecture is proportional to the drag moment (like the MEMS sensors discussed above) even though these hairs bend and are displaced at their base in the direction of the flow rather than experiencing pure rotation (as assumed in the MEMS-sensor models). The mechanical and electrical properties of CNT arrays—and therefore the resulting sensors—appear to vary in unpredictable and uncontrollable ways perhaps even more than the variation observed for MEMS devices. However, because of the simplicity of the design and approximate knowledge of the other constituent properties, a lab-bench deflection of a sensor can measure the stiffness and electromechanical response of the CNT array in order to describe the sensor response over the full operation range.

We validate the response of the calibrated sensors to steady, laminar air flow in a square flow tube of similar diameter to the length of the hairs. Inside the tube the velocity profile is nearly parabolic, varying along the length of the hair with zero velocity at the base of the hair and a maximum velocity at the tube centerline. Similarly, in boundary layer flow the velocity profile increases smoothly from zero at the surface up to the free stream velocity, so the tube serves as a model system for height-varying flow. Calculating the flow profile and using typical approximations for the drag coefficient to accurately estimate the drag forces on the hair, we show agreement between the predicted and measured response to quasi-static air flow to a degree not previously reported. The shape of the boundary layer on a wing will also vary by location and can change during flight.^[4] When integrated into an aerostructure, the length of the hairs could be adjusted to be completely enveloped in the boundary layer or extend into the freestream air flow, and arrays of spatially distributed hair sensors of varying length may have the potential to fully measure the flow over an aerodynamic

surface. Here the response of the sensors in the square tube is shown to predictably depend on hair length, both for hairs that extend above the midpoint of the tube where the air velocity is largest and for hair lengths shorter than the half width. While hair sensors have primarily been envisioned for laminar flow detection, air flow on wing surfaces can be a combination of both laminar and turbulent flow. We extend our measurements beyond the transition to turbulent air flows and observe changes in both output sensitivity and noise.

2. Results

A cross-sectional schematic of these hair-in-pore sensors is shown in **Figure 1a**. A glass microfiber is inserted into a glass capillary coated on each end with metal electrodes. A self-assembled array of carbon nanotubes is grown on the microfiber both within the capillary and on the portion of the fiber extending out of the capillary that is subjected to external forces. When the CNT-coated fiber is deflected by such forces, the array is compressed against the electrode near the top opening of the capillary which is measured as a resistance change between the top and bottom electrodes.

The observable height of the array ($L_{\text{CNT}}(x)$) is approximately equal to the length of the CNTs and can vary with axial position (x) both inside and outside the capillary.^[23] As will be discussed later, the sensitivity generally decreases with nanotube length. Also, the arrays have been observed to separate, or “mohawk,” during growth on such a small-radius fiber surface when the CNT lengths are greater than 10 μm . The small microcapillary radius was chosen to maintain radial uniformity and maximize the sensitivity of the sensors.

The growth conditions—particularly the duration of growth—determine the length of the CNTs and therefore the total diameter of the nanotube coated fiber ($D(x) = 2r + 2L_{\text{CNT}}(x)$). While $D(x)$ is typically less than or equal to the inner diameter of the capillary ($2R$), functioning sensors can also be fabricated if the CNTs are allowed to continue

growing for times longer than required to fill the capillary. The total diameter of the CNT-coated glass fiber extending outside the capillary is unconstrained and can continue to increase, while inside the capillary the hair diameter is restrained to the diameter of the capillary. In this overgrown case, the curvature of the nanotubes and density of the array inside the capillary both appear larger.

A scanning electron microscopy (SEM) image of the radial CNT array of an example sensor is shown in **Figure 1b** for which the nanotubes external to the capillary have been removed by focused ion beam. In this device the nanotubes are slightly overgrown and completely fill up the space between the capillary and the pore at the opening. However, for many of the devices discussed here, $D(x)$ at the opening of the capillary ($x = 0$) is less than $2R$. In all cases, the nanotube array mechanically supports the glass fiber down the length of the capillary and forms an electrically conductive path between the two electrodes.

The air flow response of a typical sensor mounted at the width-wise center of a tube of square cross section, 5 mm in width (see the Experimental Section), is shown in **Figure 2a**. Similar to the piezoresistive response observed for planar CNT arrays, the resistance decreases from an initial resistance (R_0) as the average air velocity is increased and saturates, or nearly saturates, at a minimum resistance (R_{sat}). This sensor was tested in four test series over the course of greater than 300 h as also shown in **Figure 2a**. There is good agreement between the response at the beginning (solid line) and end (dashed line) of each test series and the sensor appears stable for durations as long as half a day.

Comparing between test series, the sensor experiences drift over larger time frames, with both R_0 and R_{sat} changing independently. This sensor increased in resistance in each case, but other sensors have shown both increases and decreases in resistance over similar timescales. It can be seen in **Figure 2b** that the shape of the response is largely stable for the entire two weeks by normalizing each curve to both R_0 and R_{sat} according to the relationship

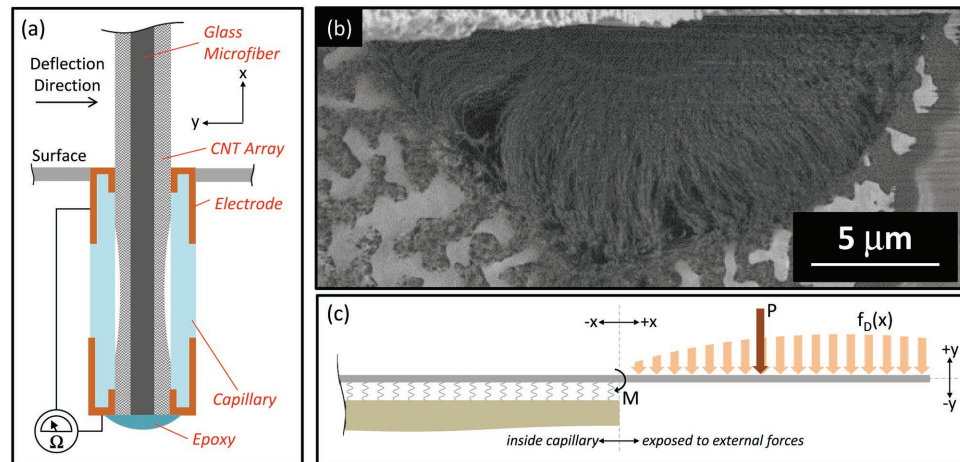


Figure 1. a) Cross-sectional schematic of nanotube-microfiber artificial hair sensor (not to scale). b) The CNT array at the opening of the capillary of a sensor below the glass fiber. A focused ion beam was used to remove the CNTs from the glass fiber. The fiber is just visible at the top of the image. c) The device can be mechanically modeled as a cantilever beam supported by a semi-infinite elastic base subjected either to point loads (P) or distributed loads ($f_D(x)$).

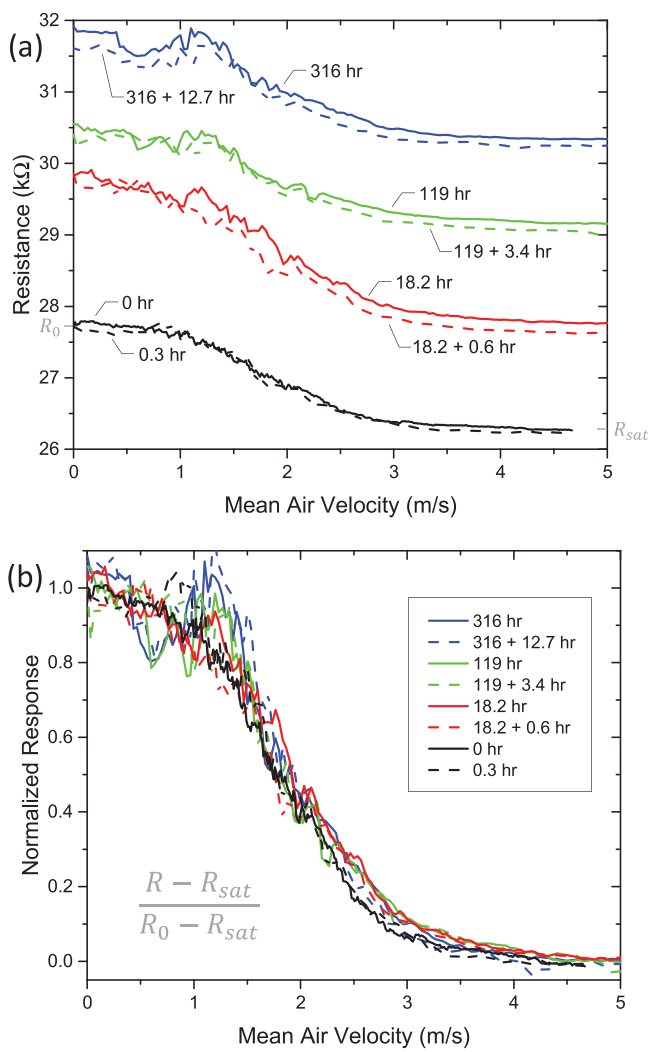


Figure 2. Response of a single sensor over time.

$$R_{norm} = \frac{R - R_{sat}}{R_0 - R_{sat}}$$

Small non-monotonic differences are still observed between the normalized response (R_{norm}) curves, especially at low air velocities, but a sigmoidal curve shape is generally maintained. In particular, the normalized slope of the linear transition region and the air velocity corresponding to this region are in good agreement between all the curves. Understanding the source of the drift is an area of future interest, but the normalized response remains sufficiently consistent over the course of lab measurements to provide predictive performance. Further, the sensor steady input-output properties defined by R_0 and R_{sat} are essentially constant for the duration of many plausible flow measurement experiments. This short and long-term stability allows the response of the sensor to

be tested and compared under the various loading conditions presented here.

If R_0 and R_{sat} are assumed to be a function of the non-transducing regions of the device (electrodes and nanotubes deep in the capillary), it is also meaningful to compare the normalized response between devices. Figure 3 shows the response of five sensors to air flow measured in the square tube setup. Perhaps surprisingly, the sensors respond differently under the same flow conditions even though the hairs are of similar length. The sensitivity for a given sensor should decrease with decreasing hair length, but that trend is not observed in comparing these sensors. In the absence of more information about the differing properties of the constituents of each sensor—specifically the properties of the nanotubes—and models to correlate those properties, it would be impossible to predict the response of each sensor. To parameterize such models, the properties of these five sensors are collected and their responses under two different loading scenarios are characterized.

The length of the nanotubes in the transducing region of the sensor at the opening of the capillary ($L_{CNT}(0)$) and the average external diameter of the hair including the contribution of the nanotubes (D_{avg}) are shown in Table 1. To determine the stiffness of the nanotube array supporting the hair inside the capillary, we compare the curvature and displacement of the hair under point loads to a partial elastic base model as has been described elsewhere.^[24,25] The CNT array supports the hair below the capillary opening ($x < 0$) while the hair above the capillary opening is free and subject to external forces (Figure 1c). While the compressive strain of the CNTs (ϵ_{CNT}) varies with angular position around the fiber, the displacement of the hair within the capillary is small and the net force on the hair is approximately linearly proportional to the local displacement of the hair.^[24] A stiffness-per-length proportionality constant (k) can be defined relative to the compressive modulus of the CNT array (κ), the inner radius of the capillary, and the radius of the glass fiber

$$k = \frac{\kappa r \pi}{2(R - r)} \quad (2)$$

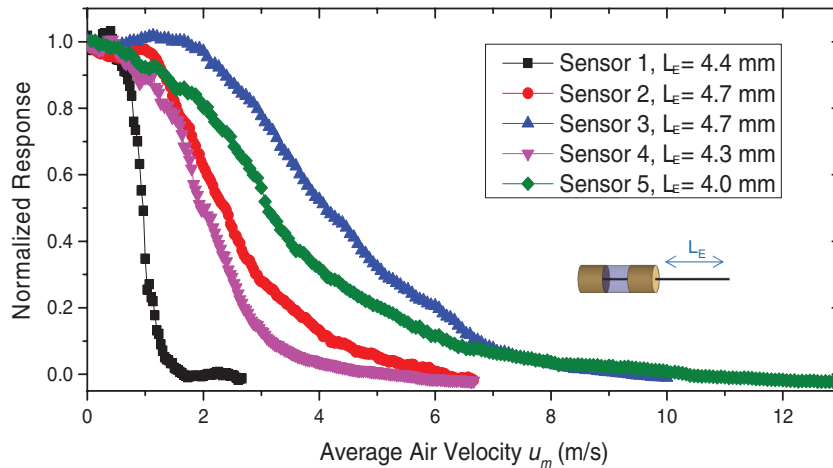


Figure 3. The air flow response of five sensors at similar exposed hair length (L_E).

Table 1. Hair sensor constituent properties. The length of the nanotubes at the opening of the capillary ($L_{\text{CNT}}(0)$) and the average diameter of the hair including the nanotubes (D_{avg}) were measured optically. The nanotube array relative stiffness factor (β) and compressive modulus (κ) were determined by fitting to the curvature of the hair under point deflections applied at various points along the hair (L_p) using Equation (8).

Sensor	$L_{\text{CNT}}(0)$ [μm]	D_{avg} [μm]	L_p [μm]	β [m^{-1}]	β standard error [m^{-1}]	R^2	K [MN m^{-2}]	κ [kPa]
1	1.8	24.9	768	6740	65	0.996	0.23	260
2	7.0	27.5	977	10300	94	0.999	1.2	1400
3	8.0	37.8	991	9310	135	0.996	0.84	950
4	5.5	36.2	851, 1120, 1320, 1410	9280	59	0.997	0.83	940
5	8.0	30.5	820, 1040, 1320, 1450, 1630, 1880, 2070	6140	18	0.997	0.16	180

The deflection anywhere along the hair can be predicted by solving the beam bending equation for the internal and external regions of the hair and including the boundary conditions that the position and slope must match at the capillary opening. A point load P applied at a distance $x = L_p$ from the capillary opening results in the following equations

$$y(x) = -\frac{P}{6EI} x^3 + \frac{L_p P}{2EI} x^2 + P \frac{1+2L_p\beta}{2EI\beta^2} x + P \frac{1+L_p\beta}{2EI\beta^3} \text{ for } x \geq 0 \quad (3)$$

$$y(x) = \frac{2\beta \exp(\beta x)}{k} [P \cos(\beta x) + L_p P \beta (\cos(\beta x) + \sin(\beta x))] \text{ for } x \leq 0 \quad (4)$$

where

$$\beta = \sqrt[4]{\frac{k}{4EI}} \quad (5)$$

using the boundary condition that the deflection of the hair goes to zero at negative infinity. This is a good approximation for these devices assuming the external load is completely transferred to the nanotube array and the deflection of the hair goes to zero far above the base of the capillary where the hair is fixed by epoxy. It is assumed that neither the CNTs nor the alumina significantly contribute to the bending stiffness (EI) of the hair. The external curvature of the hair with varying displacement is experimentally characterized and fit against Equation (3). The relative stiffness factor (β) serves as the fitting parameter, and the compressive modulus of the CNT array (κ) can be found from β by plugging Equation (2) into Equation (5).

The sensors were deflected at one or more points in x along the hair between 768 and 2070 μm and at various magnitudes in y between 0 and 100 μm (inset of Figure 4). The resulting displacement of the hair between the capillary opening and the point load were optically characterized and fit to Equation (3). The point of the deflection L_p is known in each case, leaving one independent variable P per deflection and one variable β (the relative stiffness factor) that was fit across all the deflections for a given sensor. The results are shown in Table 1. The quality of the fit is indicated by the small errors for the fit parameter β and R^2 values greater than 0.996.

The elastic base stiffness constant (k) and the compressive modulus (κ) were calculated from β using Equations (5) and (2), respectively. While all the values of κ are within the range reported for planar CNT arrays,^[20,26,27] the nanotube array properties do indeed vary from device to device as indicated by the order of magnitude differences in κ . This may be due in part to the variation in nanotube length within the capillary since the model assumes the elastic base is axially uniform and radially continuous. Regions where the nanotubes do not grow to the capillary walls would result in a reduced apparent modulus, while overgrowth of the nanotubes would increase the array density and, likewise, the apparent modulus.

Using the same apparatus, Figure 4a shows the normalized electrical response of Sensor 4 as it was deflected at various points along the hair (L_p) with magnitude of deflection (δ) ranging from 0 to 200 μm . As expected, the sensitivity to deflection decreases with increasing distance from the base of the hair. As will be discussed later, plotting the response versus the moment results in single overlapping sigmoidal curve (Figure 4b).

For comparison with the lab bench, point load calibration method of Figure 4, Figure 5 shows the responses of two of the sensors to steady, laminar air flow inside a tube with square cross section and 5 mm inner width. For each sensor, the response was collected at an initial hair length of around 4 mm. The hairs were then incrementally cut and retested to observe the change in response with decreasing hair length. As expected, as the length is reduced the sensitivity to air flow decreases. The air velocity profile is parabolic having zero value at the tube walls due to the no-slip condition and maximum value at the center of the tube. For hairs longer than the midpoint of the tube (2.5 mm), the change in sensitivity with decreasing hair length is smaller than for hairs near or below the midpoint of the tube. As was seen in Figure 3, Sensor 1 is more sensitive than Sensor 4, and this behavior is preserved through all the hair lengths.

At higher air flow rates, the flow in the tube transitions from laminar to turbulent at a Reynolds number of 2000 which corresponds to an air velocity of 6.4 m s^{-1} through this tube.^[28] The response of three sensors of differing sensitivity and hair length are shown in Figure 6. The Reynolds number was calculated using Equation (12) except with the width of the tube (5 mm) for D and the average flow velocity (u_m) for u . For each sensor, the average resistance deviates from the trend observed under laminar flow conditions, showing a decrease in sensitivity beyond $Re = 2000$. More obvious, the noise of the response measured as the RMS of the resistance sharply increases as the flow becomes turbulent.

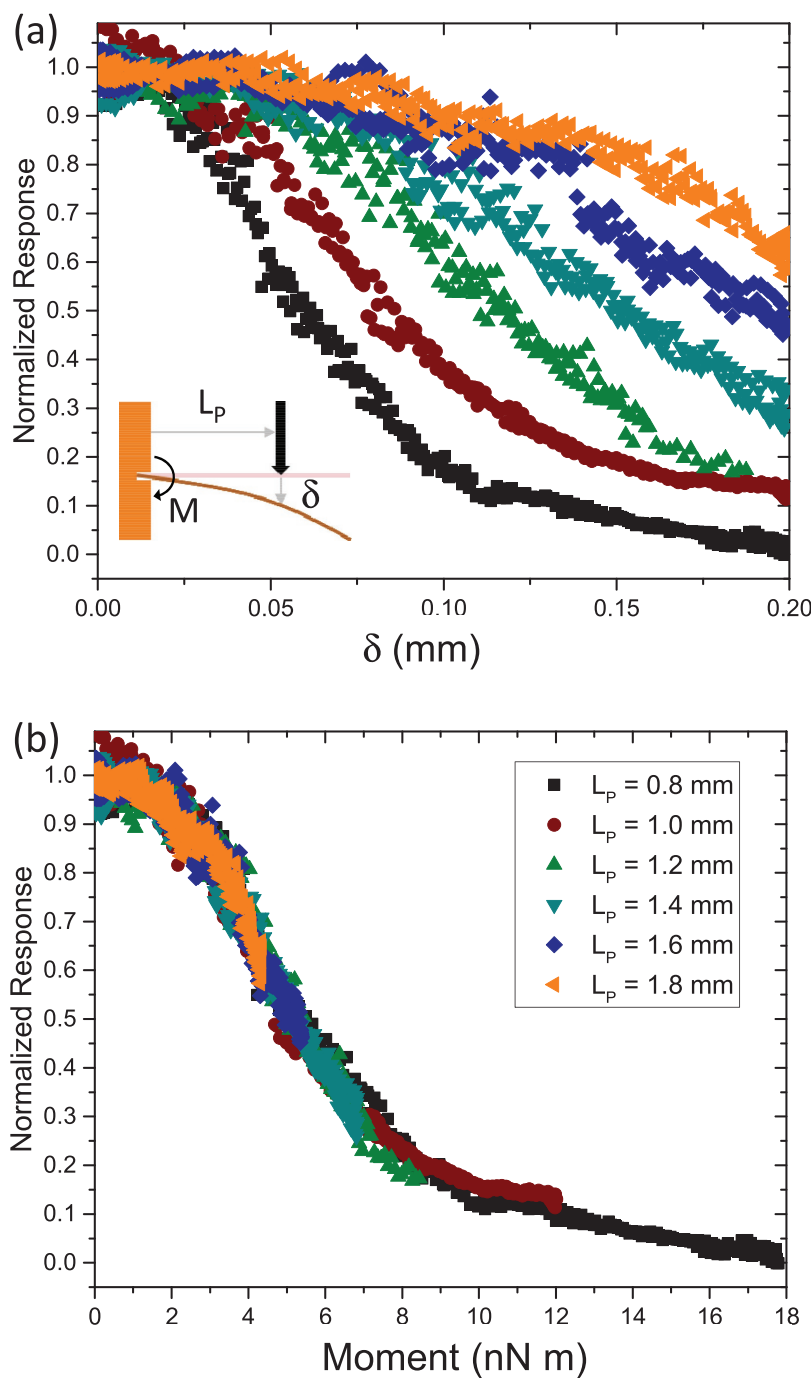


Figure 4. a) The response of Sensor 4 as the magnitude of the point deflection (δ) is increased at various points along the hair (L_p). b) The same results plotted against the calculated moment (M) about the base of the hair.

3. Discussion

For planar arrays, a sigmoidal decrease in resistance similar to that observed for these devices has been reported with increasing compressive strain against a conductive surface.^[20] As the fiber is deflected in the sensors, the nanotubes within the capillary are likewise compressed against the electrode in proportion to the local deflection of the fiber. As can be seen

from Equation (4), this deflection is nearly zero throughout the capillary and is maximized near the opening (or base of the exposed hair). Assuming the change in resistance is a function of the strain on the CNTs, the response of the sensor should be dominated by the displacement of the hair at the opening ($y(0)$) where the strain on the nanotubes is the largest.

In the case of a point load, the displacement of the fiber at the opening according to Equation (3) is

$$y(0) = P \frac{1 + L_p \beta}{2EI\beta^3} \quad (6)$$

or

$$y(0) = -M \frac{1 + L_p \beta}{2L_p EI\beta^3} \quad (7)$$

where M is the bending moment about the capillary opening

$$M = -L_p P \quad (8)$$

If L_p is much greater than $1/\beta$, then Equation (7) becomes

$$y(0) \approx -\frac{M}{2EI\beta^2} \quad (9)$$

So for forces on the hair far away from the capillary opening, the displacement of the hair at the capillary opening—and likewise the strain of the nanotube array—is proportional to the moment on the hair. Using the values for β from Table 1, this is the case for loads applied more than a few hundred micrometers from the exposed base of the hair for these sensors.

Equation (3) can be solved for the moment about the base

$$M = -\delta \frac{6EI\beta^3 L_p}{3 + 6L_p\beta + 6L_p^2\beta^2 + 2L_p^3\beta^3} \quad (10)$$

in terms of the magnitude of the applied deflection (δ). Translating the deflection to moment in Figure 4b, the response curves fall on top of each other confirming that the response of the sensors is proportional to the moment and independent of the other loading parameters.

Drag forces on the hair due to air flow will result in a distributed load along the length of the hair which will be largest where the flow velocity is largest. For monotonically increasing boundary layer flow velocity profiles, the majority of the net drag acting on the hair will also be far away from the base of the hair and the response of the sensor is expected to generally

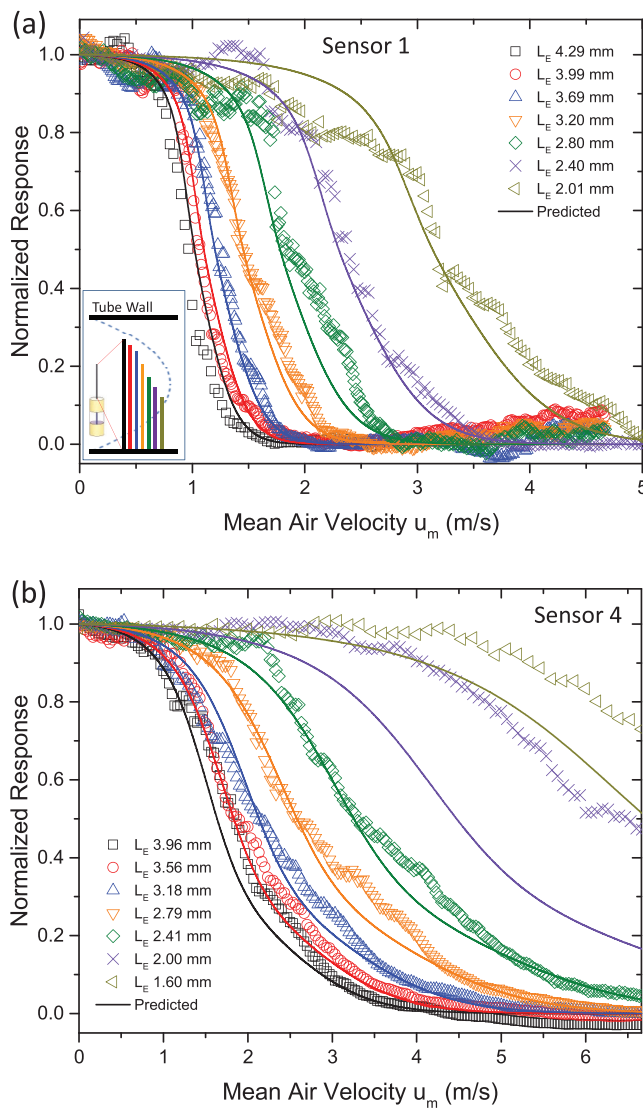


Figure 5. The discrete data points indicate the average measured air flow response of Sensor 1 a) and Sensor 4 b) at multiple exposed hair lengths (L_E). The solid lines indicate the response predicted using the point load calibration curve and the moment calculated for each length of hair. The inset shows the exposed hair lengths of Sensor 1 relative to the nearly parabolic predicted laminar air flow profile (dashed line) at the width-wise center of the square tube.

scale with the moment. It is first necessary to determine the expected interaction of the air with the sensor given the air profile within the square tube to determine the moment on the sensor due to the air flow. Once the moment is known, it should be possible to use the point load results such as the curve in Figure 4b to predict the response to air flow for the full range of operation.

For air flow sensing applications, the air exerts a distributed load on the hair due to drag. Assuming the flow velocity is perpendicular to the undeflected longitudinal axis of the hair, the force per length due to drag at a position x above the capillary opening is determined from quasi-steady aerodynamics as

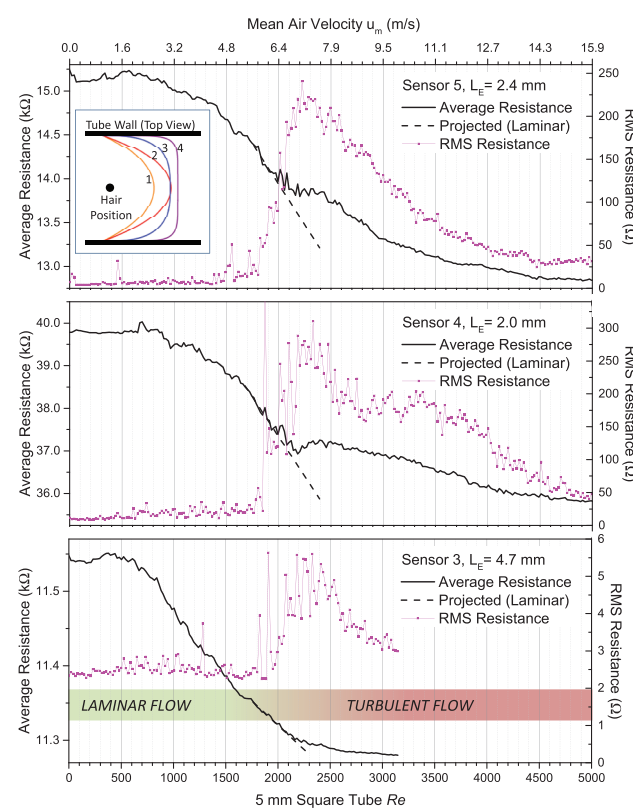


Figure 6. The response of three of the sensors as the flow in the tube transitions from laminar to turbulent. (Inset) Top down cross section of the square flow tube with plots of the approximate average air velocity profile at the vertical center of the tube for four cases, each increasing in mean air velocity over the previous: (1) typical laminar flow, (2) laminar flow just before transition to turbulence, (3) flow during transition from laminar to turbulent, and (4) fully developed turbulent flow.

$$f_D(x) = \frac{1}{2} \rho C_D(x) D(x) [u(x)]^2 \quad (11)$$

where D is the local diameter of the hair, u is the local velocity of the air, ρ is the density of the air, and C_D is the local drag coefficient which depends on the Reynolds number

$$\text{Re}(x) = \frac{D(x)u(x)}{\nu} \quad (12)$$

Note that due to the high stiffness and low viscoelasticity of the glass fiber, the aerodynamics of this particular hair sensor is quasi-steady for much higher frequency stimulus compared to devices that employ polymer.^[4] We approximate the CNT array to be non-permeable to the airflow so that the diameter of the hair $D(x)$ includes the radial CNT array. The diameter varies in x due to the non-uniform length of the nanotubes, but we find that using a constant, average diameter (D_{avg}) based on the average length of the CNTs is sufficient. For the hairs and air velocities considered here, we can expect Re values between 0.01 and 100.

For small deflections (<10% of the hair length), a circular cross section relative to the incident flow is assumed. Further,

for sufficiently high aspect ratios ($L/D > 100$) hair end effects are assumed negligible. Combined with the quasi-steady assumption, empirical formulae for quasi-steady drag coefficients over an infinitely long cylinder are valid. Other than for the creeping flow scenario ($Re \ll 1$) where analytical solutions for drag exist, empirical formulae describing the relationship between C_D and Re are determined by curve-fitting to experimental measurements of drag coefficients for circular cylinders in crossflow. For $Re < 20000$, White proposes the relationship^[29]

$$C_D(x) = 1 + 10[\text{Re}(x)]^{-\frac{2}{3}} \quad (13)$$

but for moderately small Reynolds number values ($Re < 500$) we find that the reported cylindrical drag coefficient data are better fit with slightly different coefficients

$$C_D(x) = 0.8 + 9.76[\text{Re}(x)]^{-0.674} \quad (14)$$

In using this drag coefficient we are assuming a cylindrical cross section. For large deflections of the hair the effective cross section becomes elliptical, changing the drag coefficient.

The Navier–Stokes equation can be solved with a Fourier series solution to determine the 2D air velocity profile inside a square tube, and from that the velocity profile at the midplane of the tube. The first few terms of the series are enough to adequately describe the axial velocity profile along the hair

$$u(x') \approx -\frac{56.9}{2} u_m \left[\frac{1}{8} - \frac{1}{2} \left(\frac{x'}{w} \right)^2 - \frac{4 \cos(x' \pi/w)}{\pi^3 \cosh(\pi/2)} \right],$$

$$x' = x - \frac{w}{2} \quad (15)$$

where w is the width of the tube and u_m is the mean of the velocity over the entire cross section. The 56.9 multiplier is the same value that appears in the Darcy friction factor for square tubes.

Assuming quasi-steady aerodynamics, the moment about the base of the hair due to drag is found by integrating the distributed load intensity over the exposed length of the hair

$$M = \int_0^{L_e} x f_D(x) dx \quad (16)$$

As is commonly proposed and assuming the deflections are small relative to the length of the hair, the cross section of the hair is treated as a circular cylinder. The drag force in this case due to laminar air flow in the midplane of a square tube (Equation (15)) is given in Equation (11). The equation for the moment with this drag force must be solved numerically. It is noted that the frontal, projected area of the hair is actually reduced as it is deflected, and the moment predicted by this calculation will most likely be larger than the actual moment for large deflections of the hair.

The response predicted for Sensors 1 and 4 are shown in Figure 5 (solid lines). Given the length and average diameter of the hair, the expected moment about the base of the hair was calculated at each air flow. A calibration curve of the response

to applied moment for Sensors 1 (not shown) and 4 (Figure 4b) were determined from the point load response and measured CNT array stiffness for each sensor. The predictions show good agreement with the measured responses for all lengths of Sensor 1, from 2.01 to 4.29 mm and for 0 to about 4 m s^{-1} .

Sensor 4 is less sensitive than Sensor 1 at the same hair lengths. There is good agreement for the five longest lengths of hair, but not for the hairs of length 1.60 and 2.00 mm for which the high sensitivity portion of their response curve starts above 4 m s^{-1} . It is possible that the baseline response was changed during handling or the process of cutting the hair down from 2.41 mm; however, the overestimation of the sensitivity of the hair is consistent with the approximations made in modeling the drag force.

As the flow in the tube transitions from laminar to turbulent, the sensitivity of the hairs to increasing air flow is observed to decrease as seen in Figure 6. This suggests that the resulting average moment on the hair for a given air flow is less than it would be for laminar flow. Under laminar flow conditions the flow profile is nearly parabolic across the tube with much of the flow concentrated near the center of the tube where the hair sensor is located. Under turbulent flow conditions the flow is more evenly distributed or constant across the cross section of the tube, decreasing to zero sharply near the edges.^[30] As the flow transitions from laminar to turbulent at $Re = 2000$, the transition between the associated flow profiles is expected to result in a large increase in average flow velocity near the edges; whereas, the flow at the center of the tube should remain somewhat constant or may even initially decrease (inset of Figure 6). Even though the mean flow through the tube continues to increase, the flow seen by the hair and resulting moment on the hair change very little until the turbulent flow is more fully developed.

In addition to a decrease in sensitivity measured in the average response of the sensor, the noise of the response is observed to be larger under turbulent flow conditions presumably due to the fluctuations in air velocity characteristic of turbulent flow. Based on the change in resistance per change in average air velocity under laminar conditions near the transition, the RMS magnitude of the fluctuations is determined to be 1%–2% of the average air velocity at $Re = 2000$ for all three sensors in Figure 6 which is within the range expected for turbulent flow.^[30] Fourier analysis of the fluctuations of the sensor response shows them to exhibit a $1/f$ power-law scaling versus frequency with a broadband increase in amplitude during the transition from laminar to turbulent flow (Supporting Information). Peaks in the Fourier amplitude are observed near frequencies corresponding to the resonance modes of the hairs (measured independently) especially around 1 kHz, otherwise no characteristic frequencies are observed between 10 Hz and 10 kHz.

At an average velocity of 6.4 m s^{-1} corresponding to a Reynolds number of the tube of 2000, the Reynolds numbers of the hairs are less than 20. The hairs are therefore not expected to further contribute to the turbulent flow. Vortex shedding is predicted for cylinders at Reynolds numbers above about 40 and can produce an oscillation in the drag force on the cylinder.^[30] For these hairs a $Re = 40$ corresponds to an average velocity greater than 16 m s^{-1} which is beyond the velocities considered

here. Even then it would be difficult to detect their contribution in our setup as the vortex shedding frequency at such a velocity is expected to be above 1 MHz. At the air velocities considered here, the increased noise of the sensor is due to the turbulent flow induced by the tube rather than an effect of the hair on the flow.

While the moment response differs from one sensor to another, we have shown that the expected response can be translated from one loading scenario to another if the magnitude of the moment is known in both cases. Looking toward incorporating large numbers of sensors into arrays for spatial flow mapping, it is feasible to envision calibrating their full response by measuring the point deflection response of each sensor.

The only factor from Equation (10) that cannot be measured simply or easily from automated methods is β , or the nanotube array stiffness factor. While the process for determining β from the curvature of the deflected hair described earlier could be automated, it may not prove as feasible for large numbers of sensors. An alternate method is presented here. Starting with the assumption that the response of the sensors is dependent on moment and independent of the loading parameters (for loads away from the base of the hair), the correct value of β is that which forces the point deflection response curves for differing values of L_p (such as those in Figure 4) to collapse to the same moment response curve (as they do in Figure 4b).

Going further, it is desirable to predict the sensor response purely from measurable quantities and, ultimately, to control for these properties during fabrication of the sensors to predetermine their performance. The sensors have been shown to have a characteristic, somewhat sigmoidal response to moment, with the resistance decreasing linearly over the range of maximum sensitivity

$$\gamma_{\text{sensor}} \equiv -\frac{\Delta R_{\text{norm}}}{\Delta |M|} \quad (17)$$

It was suggested previously that the response of the sensor is primarily due to the strain of the nanotubes near the opening of the capillary, proportional to the ratio of the displacement of the hair and length of the nanotubes

$$\varepsilon_{\text{CNT}}(0) \approx \frac{y(0)}{L_{\text{CNT}}(0)} \quad (18)$$

The change in resistance of the CNT array likewise varies sigmoidally with strain, with an approximately linear response over the region of maximum sensitivity. Over this region, this response takes on the typical form

$$GF_{\text{CNT}} \equiv -\frac{1}{R_0} \frac{\Delta R}{\Delta \varepsilon_{\text{CNT}}} \quad (19)$$

where GF_{CNT} is the piezoresistive gauge factor of the nanotube array and ε_{CNT} is the compressive strain on the CNTs. The CNT subscript is used to designate these factors as properties of CNT arrays rather than the sensor. In terms of the normalized resistance, the maximum normalized piezoresistivity can be defined as

$$\gamma_{\text{CNT}} \equiv -\frac{\Delta R_{\text{norm}}}{\Delta \varepsilon_{\text{CNT}}} = \frac{R_0}{R_0 - R_{\text{sat}}} GF_{\text{CNT}} \quad (20)$$

Combining these equations with Equation (9), the normalized sensor sensitivity can be written as

$$\gamma_{\text{sensor}} = \frac{1}{2} \gamma_{\text{CNT}} \frac{1}{EI} \frac{1}{\beta^2 L_{\text{CNT}}(0)} \quad (21)$$

which is a function of a value that is constant across all the sensors (EI), two properties that can be measured for each sensor (β and L_{CNT}), and one property that cannot yet be directly measured (γ_{CNT}).

Noting that the sensor sensitivity should increase with decreasing nanotube length, 20 additional sensors were fabricated with shorter nanotubes. The point deflection response was collected at L_p values of 600, 800, and 1000 μm for each sensor. The nanotube array stiffness factor β was determined by collapsing the point deflection response curves onto the same moment response curve as suggested earlier in this section. The average length of the nanotubes at the capillary opening was 1.8 μm and the average β was 3050 m^{-1} with an average standard error of 98 m^{-1} by this method.

The normalized moment sensitivity for these 20 sensors and the five original sensors is plotted against the length of the nanotubes and β for each of the sensors according to Equation (21) along with a linear fit in Figure 7. Decreasing the length of the nanotubes increased the normalized sensitivity as much as two orders of magnitude. The scatter may be due to the error in measuring the nanotube stiffness, length, or due to the variation of γ_{CNT} . For values of $L_{\text{CNT}}^{-1}\beta^{-2}$ less than about 0.1 m, the sensitivity increases somewhat linearly as predicted. For smaller lengths and stiffness values (larger values of $L_{\text{CNT}}^{-1}\beta^{-2}$), the scatter is large and the linear dependence is less evident. This deviation may be due to the error in measuring the nanotube stiffness or length, or it may be due to the underlying variation of γ_{CNT} . Further, these lengths and stiffness values correspond to a relatively sparse and soft nanotube array supporting the fiber down the length of the capillary which may differ from the assumptions of the elastic base mechanical model. A dashed line corresponding to the logarithmically

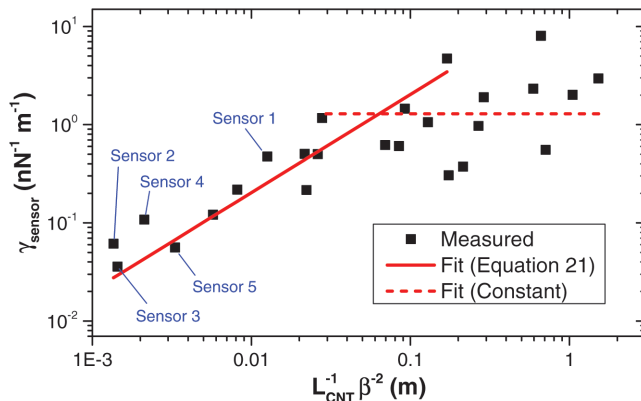


Figure 7. The normalized moment sensitivity (γ_{sensor}) for 25 sensors versus the nanotube stiffness factor (β) and the length of the CNTs (L_{CNT}) at the opening of the capillary.

weighted average of these points ($1.3 \pm 0.4 \text{ nN}^{-1} \text{ m}^{-1}$) is plotted and serves as a prediction of the maximum normalized sensitivity that can be reasonably expected for this architecture.

The solid line in Figure 7 was found by fitting Equation (21) to the points for sensors with longer, stiffer CNTs ($L_{\text{CNT}}^{-1}\beta^{-2} < 0.1 \text{ m}$). The slope of line corresponds to a value of 1.1 for the unit-less, normalized strain sensitivity of the underlying CNT array (γ_{CNT}) with a standard error of 0.2. Plugging this value back into Equation (21), it may be possible to predict the performance of future sensors without the need for calibration. While γ_{CNT} is related to the gauge factor, the normalization process removes information about the resistance values required to calculate GF_{CNT} ; moreover, the initial resistance R_0 (and therefore GF_{CNT}) has been shown to change over large timescales while γ_{CNT} remains constant. For comparison, we determined a γ_{CNT} of about 24 from the strain-resistance results reported by Maschmann et al. for compression measurements of a 12 μm tall planar CNT array.^[20] The smaller value of γ_{CNT} observed for our devices may be a difference in the properties of radial versus planar CNT arrays, or we may be underestimating γ_{CNT} by only considering the strain of the CNTs experiencing the largest compression.

4. Conclusion

We have demonstrated these CNT-based artificial hair sensors can be systematically characterized and calibrated under controlled, benchtop conditions such as with a point load, resulting in the ability to predict their response to steady airflows. The models used here to calculate the drag forces have been suggested elsewhere and are valid for small deflections of the hair. Differing from other sensors and measurements, these sensors are highly sensitive to small deflections, and the airflow inside the flow tube was well controlled and is well understood. Although the analysis and characterization here are for steady flows, we expect it to also be valid for high-frequency dynamic loading due to the small diameter of the hair structure and its high elasticity.

The nature of the compressive modulus and piezoresistivity in carbon nanotube arrays is still not yet able to be correlated to synthesis conditions. While the elastic base stiffness varied between devices by about an order of magnitude, the normalized piezoresistivity—or percent of the maximum resistance change per change in percent strain—of the CNT arrays was observed here to be about 1.1 across all devices of sufficient CNT length and stiffness. While the value obtained here may be device-dependent, the normalized piezoresistivity may prove to be an intrinsic, constant property of CNT arrays.

The nominal and saturation resistances are partially a function of the electrical path down the shaft of the capillary through the nanotubes that are largely undeformed even as the hair is deflected. The drift in these values might be due to temperature or humidity changes which could produce changes in CNT-CNT interconnectivity or thermal deformation. It is not known whether such drift is observed in planar arrays. Given the stability of these values for over 12 h and the stability of the normalized response of over two weeks, in an ongoing application we envision re-characterizing the undeflected and fully

deflected resistance of the sensors at the beginning of each day of use to remove the influence of this effect.

It was also demonstrated that the sensors can be used to detect the transition of flow from laminar to turbulent with a change in their average sensitivity to increasing air flow and a sharp increase in their otherwise constant RMS noise. The change in sensitivity is an indication of the changing average flow distribution, and the fluctuations in the response of the sensors indicate the ability of the sensors to detect the turbulent flow fluctuations about the mean flow. The flow over a wing can be laminar or turbulent, attached or separated, and wool tufts attached to the wing are sometimes used to visualize these flows. Likewise, it may be possible to use the sensors to detect and map these conditions electrically.

As has been theorized for other sensor architectures, the response of these sensors was shown to be a function of the moment about the base of the hair resulting from the net forces on the hair. In boundary layer flow applications, the shape of the velocity profile may change during operation such that the same moment could be produced for different free stream velocities. Readout of the sensors may require real-time access to accurate models of the boundary layer under various conditions, or it may be possible to use hairs of different lengths to sample different portions of the boundary layer. In addition to structure–property relationships for the sensors and processes for zeroing or normalizing for long-term drift like those demonstrated here, more complete drag models may be required for sensors that operate at large deflection where the small angle assumptions made here are no longer valid.

5. Experimental Section

Sensor Fabrication: The hairs of the sensors are glass microfibers (AGY 933 S-2) with a radius (r) of 4.5 μm , density (ρ) of 2580 kg m^{-3} , and bending stiffness (EI) of 28 $\text{N } \mu\text{m}^2$. The fibers were uniformly coated with $\approx 10 \text{ nm}$ of alumina by atomic layer deposition (Cambridge NanoTech). The pore for the hair is a glass microcapillary (Polymicro Technologies) with off-the-shelf inner radius (R) of 12.5 μm which was cut and polished to a final length of $\approx 1.2 \text{ mm}$ (typical). Gold electrodes were deposited by mounting numerous capillaries on end in a holder and sputtering at an angle such that the gold coats the inside walls of the capillaries to a depth approximately equal to twice the diameter. The process was repeated for the opposite end of the capillaries. The faces and sides on both ends were also coated but the middle of the capillary was not. The holder acts as a physical mask, blocking the deposition in the middle to electrically isolate the two ends. The glass fibers were cut to the desired length and inserted into the microcapillaries.

The entire assemblies were subjected to CNT synthesis in a tube furnace at 750 °C by continuous liquid injection of a ferrocene/xylene mixture that vaporizes near the opening of the furnace and was transported to the sample with argon and hydrogen gases.^[18,23,25] The CNTs grow preferentially on the alumina-coated glass fiber and radially from the fiber surface as a low density array of wavy, vertically aligned, entangled CNTs. As it grows, the CNT array self-positions the glass fiber near the radial center of the capillary. Finally, the hair was fixed to the bottom face of the capillary with epoxy to prevent axial movement.

Point Load Measurements: A custom benchtop fixture was fabricated to test the electrical response of the sensor and the curvature and displacement of the hair to point loads. The hair was deflected by a razor blade and the magnitude of the deflection was changed by a microactuator either incrementally or continuously at a typical rate of 20 $\mu\text{m s}^{-1}$. The load was applied from the side to allow for optical

microscope imaging of the load position and hair profile. A constant voltage of 100 mV was applied to the device and the resulting current was collected—both with a Keithley 2400 sourcemeter—at a rate of about 10 Hz and correlated to the position of the microactuator and optical images.

Measurements in the Flow Tube: A 1 m long, 5 mm square inner diameter aluminum alloy tube connected on both ends to 8 m of copper pipe was used to test the response to air flow. The system was modeled after the hybrid plane-wave tube setup described by Chandrasekaran et al.^[31] but here it is used to create known, steady parabolic flow stimuli. The sensor was mounted at the lengthwise and widthwise center of the tube, downstream of the transition region at the entrance, so that the flow is fully developed. The top of the sensor microcapillary (base of the exposed hair) was mounted flush with the inner bottom surface of the inside of the tube. The average air velocity (u_m) was stepwise increased with a mass flow controller, verified by measuring the pressure drop along the length of the tube. The sensor resistance was measured at 20 kHz for a duration of 2 s at each flow, recorded by a National Instruments Signal Acquisition Module NI PXI-6224.

Supporting Information

Supporting Information is available from the Wiley Online Library or from the author.

Acknowledgements

The authors gratefully acknowledge financial support from the Air Force Office of Scientific Research (AFOSR), Dr. Byung-Lip (Les) Lee, Program Manager, Peter Schuhmann for assistance with data collection in the square tube, and Matthew Maschmann for focused ion beam processing and imaging of the sensor in Figure 1. The reference to the equation in figure 7 was incorrectly presented in the originally published manuscript. This was corrected on December 14, 2016.

Received: August 10, 2016
Revised: September 19, 2016

Published online: November 7, 2016

- [1] Y. Ozaki, T. Ohyama, T. Yasuda, I. Shimoyama, presented at *13th Annual Int. Conf. Micro Electro Mechanical Systems (MEMS 2000)*, Miyazaki, Japan, January **2000**, pp. 531–536.
- [2] Z. Fan, J. Chen, J. Zou, D. Bullen, C. Liu, F. Delcomyn, *J. Micromech. Microeng.* **2002**, *12*, 655.
- [3] B. T. Dickinson, J. Singler, B. A. Batten, presented at *3rd AIAA Flow Control Conf.*, San Francisco, California, June **2006**.
- [4] B. T. Dickinson, *Bioinspiration Biomimetics* **2010**, *5*, 016002.
- [5] Y.-H. Wang, C.-Y. Lee, C.-M. Chiang, *Sensors* **2007**, *7*, 2389.
- [6] Q. Zhang, W. Ruan, H. Wang, Y. Zhou, Z. Wang, L. Liu, *Sens. Actuators, A* **2010**, *158*, 273.

- [7] L. Du, Z. Zhao, C. Pang, Z. Fang, *Sens. Actuators, A* **2009**, *151*, 35.
- [8] N. Chen, C. Tucker, J. M. Engel, Y. Yingchen, P. Saunvit, L. Chang, *J. Microelectromech. Syst.* **2007**, *16*, 999.
- [9] H. Droogendijk, J. Casas, T. Steinmann, G. Krijnen, *Bioinspiration Biomimetics* **2014**, *10*, 016001.
- [10] M. Dijkstra, J. J. v. Baar, R. J. Wiegerink, T. S. J. Lammerink, J. H. d. Boer, G. J. M. Krijnen, *J. Micromech. Microeng.* **2005**, *15*, S132.
- [11] T. Shimozawa, T. Kumagai, Y. Baba, *J. Comp. Physiol., A* **1998**, *183*, 171.
- [12] G. Krijnen, A. Floris, M. Dijkstra, T. Lammerink, R. Wiegerink, presented at *SPIE Bioengineered and Bioinspired Systems III*, Maspalomas, Gran Canaria, May **2007**, 65920F, DOI: 10.1117/12.721807.
- [13] A. G. P. Kottapalli, M. Bora, M. Asadnia, J. Miao, S. S. Venkatraman, M. Triantafyllou, *Sci. Rep.* **2016**, *6*, 19336.
- [14] H. Droogendijk, A. M. K. Dagamseh, R. G. P. Sanders, D. R. Yntema, G. J. M. Krijnen, *Meas. Sci. Technol.* **2014**, *25*, 095005.
- [15] T. Nima, A. S. Stephen, *Bioinspiration Biomimetics* **2016**, *11*, 036008.
- [16] T. Junliang, Y. Xiong, *Smart Mater. Struct.* **2012**, *21*, 113001.
- [17] F. G. Barth, *Zoology* **2002**, *105*, 271.
- [18] M. R. Maschmann, G. J. Ehlert, B. T. Dickinson, D. M. Phillips, C. W. Ray, G. W. Reich, J. W. Baur, *Adv. Mater.* **2014**, *26*, 3230.
- [19] D. M. Phillips, C. W. Ray, B. J. Hagen, W. Su, J. W. Baur, G. W. Reich, *Smart Mater. Struct.* **2015**, *24*, 115026.
- [20] M. R. Maschmann, B. Dickinson, G. J. Ehlert, J. W. Baur, *Smart Mater. Struct.* **2012**, *21*, 094024.
- [21] G. J. Ehlert, M. R. Maschmann, J. W. Baur, presented at *SPIE Active and Passive Smart Structures and Integrated Systems*, San Diego, California, March **2011**, p. 79771C.
- [22] J. Suhr, P. Victor, L. Ci, S. Sreekala, X. Zhang, O. Nalamasu, P. M. Ajayan, *Nat. Nanotechnol.* **2007**, *2*, 417.
- [23] K. Slinker, M. R. Maschmann, C. Kondash, B. Severin, D. Phillips, B. T. Dickinson, G. Reich, J. Baur, presented at *SPIE Smart Structures/NDE*, San Diego, California, March **2015**, p. 942917–13, DOI: 10.1117/12.2085568.
- [24] K. Slinker, C. Kondash, M. Maschmann, B. Severin, G. Reich, B. T. Dickinson, J. Baur, presented at *20th Int. Conf. Composite Materials*, Copenhagen, July **2015**.
- [25] D. M. Phillips, K. A. Slinker, C. W. Ray, B. J. Hagen, J. W. Baur, B. T. Dickinson, G. W. Reich, presented at *ASME 2014 Conference on Smart Materials, Adaptive Structures and Intelligent Systems*, Newport, Rhode Island, September **2014**, V002T06A016. DOI: 10.1115/smasis2014-7707.
- [26] Y. Gao, T. Kodama, Y. Won, S. Dogbe, L. Pan, K. E. Goodson, *Carbon* **2012**, *50*, 3789.
- [27] M. R. Maschmann, G. J. Ehlert, S. Tawfick, A. J. Hart, J. W. Baur, *Carbon* **2014**, *66*, 377.
- [28] H. Tennekes, J. L. Lumley, *A First Course in Turbulence*, MIT Press, Cambridge, Massachusetts, **1972**.
- [29] F. M. White, *Viscous Fluid Flow*, McGraw-Hill, New York Vol. xix, New York **1974**, p. 725.
- [30] F. M. White, *Fluid Mechanics*, McGraw-Hill, New York **1979**.
- [31] V. Chandrasekaran, A. Cain, T. Nishida, L. N. Cattafesta, M. Sheplak, *Exp. Fluids* **2005**, *39*, 56.